Topological phase transitions in small mesoscopic chiral *p*-wave superconductors

L.-F. Zhang, L. Covaci, and M. V. Milošević[*]

Departement Fysica, Universiteit Antwerpen, Groenenborgerlaan 171, B-2020 Antwerpen, Belgium

(Received 23 October 2017; revised manuscript received 4 December 2017; published 26 December 2017)

Spin-triplet chiral *p*-wave superconductivity is typically described by a two-component order parameter, and as such is prone to unique emergent effects when compared to the standard single-component superconductors. Here we present the equilibrium phase diagram for small mesoscopic chiral *p*-wave superconducting disks in the presence of magnetic field, obtained by solving the microscopic Bogoliubov–de Gennes equations self-consistently. In the ultrasmall limit, the cylindrically symmetric giant-vortex states form the ground state of the system. However, with increasing sample size, the cylindrical symmetry is broken as the two components of the order parameter segregate into domains, and the number of fragmented domain walls between them characterizes the resulting states. Such domain walls are topological defects unique for the *p*-wave order, and constitute a dominant phase in the mesoscopic regime. Moreover, we find two possible types of domain walls, identified by their chirality-dependent interaction with the edge states.

I. INTRODUCTION

Superconductors described by multicomponent order parameters have drawn a lot of attention over the last few decades [1–3]. They exhibit many interesting properties that are not possible in the conventional single-component superconductors, such as collective Leggett modes [4], fractional vortices [5], skyrmionic knotted solitons [6], phase solitons [6–8], and hidden criticality [9], to name a few.

Of particular interest are the spin-triplet chiral *p*-wave superconductors with the multicomponent order parameter of type $\Delta_\pm(p) \sim p_x \pm i p_y$ [10,11]. Such symmetries can be realized in the A phase of superfluid ^{3}He [12] and may be attributed to the layered ruthenate superconductor Sr_2RuO_4 [13]. Such an order parameter breaks the time-reversal symmetry (TRS), indicating that Cooper pairs carry internal angular momentum. For this reason, chiral *p*-wave superconductors can support rich topological defect states with exotic physical properties. For example, a vortex exhibits different properties depending on whether its vorticity is parallel or antiparallel to the internal angular momentum of the Cooper pairs [14–16]. Further, one finds that domains of different chiralities, namely, $p_x + i p_y$ and $p_x - i p_y$, are degenerate in energy and therefore can coexist in the ground state, separated by a chiral domain wall (DW)—a topological defect unique to chiral superconductivity [17–20]. Such a domain wall is attractive for half-quantum vortices [21], and when enclosed it can form a so-called coreless vortex, with skyrmionic topological properties [22–24].

Another important aspect of chiral *p*-wave superconductivity is its nontrivial topological order [11], analogous to that of the Moore-Read state for quantum Hall systems at 5/2 filling [25]. A consequence of that topological order is the existence of Majorana zero modes [26], which obey non-Abelian statistics and hold promise for realization of a topological quantum computer. A well-known example is that the half-quantum vortex in a chiral *p*-wave superconductor supports a single Majorana zero mode at its core [27]. However, the half-

quantum vortex is thermodynamically unfavorable because its energy diverges logarithmically with the size of the system due to unscreened spin currents. Therefore, one possible way to stabilize such half-quantum vortices is to employ mesoscopic confinement. The evidences for the existence of half-quantum vortices in a mesoscopic Sr_2RuO_4 ring [28], as well as in trapped superfluid ^{3}He [29], have recently been reported.

Mesoscopic superconducting systems, the dimensions of which are comparable to the penetration depth and the coherence length, often serve as a platform to investigate the fundamental physics of topological defect states. Vortex states in confined conventional superconductors have been well studied over the past few decades [30–34], with emphasis on their dependence on the size and geometry of the sample. For example, a coalescence of a multivortex state into a giant vortex (one vortex but carrying multiple flux quanta) under influence of mesoscopic confinement was predicted and observed experimentally [31,35,36]. In multicomponent superconductivity, mesoscopic samples are expected to stabilize fractional vortices [37], which are thermodynamically unfavorable in bulk samples. However, the emergent states in mesoscopic chiral *p*-wave superconductors are still under debate. For example, Refs. [38,39] show contradictory results for small mesoscopic *p*-wave disks, even in the absence of external magnetic field. For that reason, in this paper we study possible states in small mesoscopic chiral *p*-wave superconducting disks by solving the microscopic Bogoliubov–de Gennes (BdG) equations self-consistently, in two dimensions, without any unnecessary assumption. We find that, in contrast to the vortex states always forming the ground state in ultimately small disks, domain-wall states form the ground state in larger mesoscopic samples. These domain walls appear upon splitting of the composite vortex, which has coinciding vortex (or antivortex) cores in each component of the order parameter. In terms of symmetry breaking, this phase transition is similar to the one between giant vortex states and multivortex states in *s*-wave superconductors. These novel states made of domain walls and their interplay with vortices in the mesoscopic limit are unique to *p*-wave order, and therefore relevant to several recently realized systems with *p*-wave-like topological superconductivity [40–43]. The only such mesoscopic system

---
[*]milorad.milosevic@uantwerpen.be

to date is the nanoscale Pb/Co/Si(111) hybrid of Ref. [44], in which the chiral edge modes were observed and where the dependence of the ground state on the size of the system and the applied magnetic field can be directly explored, with an eye on stabilization and observation of the Majorana bound states within the emergent topological defects.

The paper is organized as follows. In Sec. II we introduce our theoretical (Bogoliubov–de Gennes) formalism for p-wave superconductors, allowing for noncylindrically symmetric states. In Sec. III we present the results of our simulations, reporting the equilibrium phase diagram of emergent topological-defect states as a function of the applied field and the size of the mesoscopic p-wave system, with thorough investigation of all found states and transitions between them. Our findings are summarized in Sec. IV.

II. THEORETICAL FORMALISM

The order parameter with chiral p-wave pairing symmetry can be expressed as

$$\Delta(\mathbf{r},\mathbf{k}) = \Delta_+(\mathbf{r})Y_+(\mathbf{k}) + \Delta_-(\mathbf{r})Y_-(\mathbf{k}). \quad (1)$$

Here $\Delta_\pm(\mathbf{r})$ are the spatial $p_x \pm ip_y$-wave order parameters and $Y_\pm(\mathbf{k}) = (k_x \pm ik_y)/k_F$ are the pairing functions in relative momentum space. The spinless BdG equations are written as [45]

$$\begin{bmatrix} H_e(\mathbf{r}) & \Pi(\mathbf{r}) \\ -\Pi^*(\mathbf{r}) & -H_e^*(\mathbf{r}) \end{bmatrix} \begin{bmatrix} u_n(\mathbf{r}) \\ v_n(\mathbf{r}) \end{bmatrix} = E_n \begin{bmatrix} u_n(\mathbf{r}) \\ v_n(\mathbf{r}) \end{bmatrix}, \quad (2)$$

where

$$H_e(\mathbf{r}) = \frac{1}{2m_e} \left[\frac{\hbar}{i}\nabla - \frac{e}{c}\mathbf{A}(\mathbf{r}) \right]^2 - E_F \quad (3)$$

is the single-particle Hamiltonian with m_e being the electron mass, E_F the Fermi energy, and $\mathbf{A}(\mathbf{r})$ the vector potential. We use the gauge $\nabla \cdot \mathbf{A} = 0$. For simplicity, we consider a cylindrical two-dimensional Fermi surface. In addition, the contribution of the supercurrent to the total magnetic field can be neglected in thin superconducting samples [23], resulting in a vector potential of form $\mathbf{A}(\mathbf{r}) = \frac{1}{2}H_0 r \mathbf{e}_\theta$, with the applied magnetic field $\mathbf{H} = H_0\mathbf{e}_z$. Term $\Pi(\mathbf{r})$ is written as

$$\Pi(\mathbf{r}) = -\frac{i}{k_F}\sum_\pm \left[\Delta_\pm \Box_\pm + \frac{1}{2}(\Box_\pm\Delta_\pm) \right], \quad (4)$$

with $\Box_\pm = e^{\pm i\theta}(\partial_r \pm \frac{i}{r}\partial_\theta)$ in cylindrical coordinates. $u_n(\mathbf{r})(v_n(\mathbf{r}))$ are electron(hole)-like quasiparticle eigenfunctions obeying the normalization condition

$$\int |u_n(\mathbf{r})|^2 + |v_n(\mathbf{r})|^2 d\mathbf{r} = 1, \quad (5)$$

and E_n are the corresponding quasiparticle eigenenergies. The system is considered to be a disk of radius R, therefore the boundary conditions for the wave functions are $u_n(r = R) = 0$ and $v_n(r = R) = 0$. The order parameters, $\Delta_\pm(\mathbf{r})$, satisfy the self-consistent gap equations

$$\Delta_\pm(\mathbf{r}) = -i\frac{g}{2k_F}\sum_{E_n<\hbar\omega_D} [v_n^*(\mathbf{r})\Box_\mp u_n(\mathbf{r}) - u_n(\mathbf{r})\Box_\mp v_n^*(\mathbf{r})]$$
$$\times [1 - 2f_n], \quad (6)$$

where $k_F = \sqrt{2mE_F/\hbar^2}$ is the Fermi wave number, g is the superconducting coupling strength, and $f_n = f(E_n) = [1 + \exp(E_n/k_BT)]^{-1}$ is the Fermi-Dirac distribution function. The summation in Eq. (6) is over all the quasiparticle states with energies in the Debye window, $\hbar\omega_D$. Due to the $p_x \pm ip_y$ symmetry, the angular momentum can take the values ± 1, and the phase winding numbers $L_\pm$ of $\Delta_\pm$ always preserve the relative relation $L_- = L_+ + 2$.

To solve the previous equations, we expand the quasiparticle wave functions, $u_n(\mathbf{r})$ and $v_n(\mathbf{r})$, in terms of a complete orthonormal basis set:

$$\begin{pmatrix} u_n(\mathbf{r}) \\ v_n(\mathbf{r}) \end{pmatrix} = \sum_{\mu j} \begin{pmatrix} c_{\mu j}^n \\ d_{\mu j}^n \end{pmatrix} \varphi_{j\mu}(r,\theta), \quad (7)$$

where $c_{\mu j}^n$ and $d_{\mu j}^n$ are coefficients, $\mu \in \mathbb{Z}$ are angular quantum numbers corresponding to the angular momentum operator, and the basis functions

$$\varphi_{j\mu}(r) = \frac{\sqrt{2}}{RJ_{\mu+1}(\alpha_{j\mu})}J_\mu\left(\alpha_{j\mu}\frac{r}{R}\right)\frac{e^{i\mu\theta}}{\sqrt{2\pi}}, \quad (8)$$

with J_μ the μth Bessel function and $\alpha_{j\mu}$ the jth zero of J_μ. The BdG equations can now be reduced to a matrix eigenvalue problem. Here, we do not impose the cylindrical symmetry on the order parameters. Therefore, $\Delta_\pm$ have the general form $\Delta_\pm = \sum_m \Delta_\pm(r)e^{im\theta}$.

To construct the ground-state phase diagram, we calculate the free energy at each self-consistent iteration step (see Appendix A for more details) as

$$\mathcal{G} = \sum_n \left\{ 2E_n f_n - 2E_n \int d\mathbf{r}|v_n|^2 \right.$$
$$\left. - \int d\mathbf{r}[u_n^*\tilde{\Pi}v_n f_n + v_n\tilde{\Pi}u_n^*(1 - f_n)] \right\} - TS. \quad (9)$$

Here $S = k_B[f_n \ln f_n + (1 - f_n)\ln(1 - f_n)]$ is the electronic entropy and $\tilde{\Pi} = 2\Pi - \Pi'$, where Π is calculated using Eq. (4) with the initial input of $\Delta_\pm$ but in Π' the order parameters $\Delta_\pm$ are calculated according to Eq. (6). The free energy $\mathcal{G}$ given by Eq. (9) is valid during all self-consistent iteration steps so that one can find that $\mathcal{G}$ always decreases with iterations. Once the self-consistence loop converges, we also obtain $\tilde{\Pi} = \Pi$. The magnetic energy has been neglected since we consider a thin sample. For convenience, we define the superconducting free-energy density G with respect to the corresponding normal state one, i.e.,

$$G = (\mathcal{G} - \mathcal{G}_N)/A, \quad (10)$$

where $\mathcal{G}_N$ is the free energy of the normal state (i.e., $\Delta_\pm \equiv 0$) and $A = \pi R^2$ is the area of the disk sample. The corresponding bulk superconducting free-energy density at zero temperature ($T = 0$) in absence of magnetic field ($\phi = 0$) is denoted as G_0.

Without particular loss of generality, and taking into account numerical convenience, the parameters used in this paper are $E_F = \hbar\omega_D \approx 27\Delta_0$ [46], resulting in (1) $k_F\xi_0 \approx 18$, where $\xi_0 = \hbar v_F/\pi\Delta_0$ is the BCS coherence length at zero temperature, with $v_F(k_F)$ the Fermi velocity (wave number) and Δ_0 the bulk order-parameter amplitude at zero temperature, and (2) $\Delta_0/k_BT_c = 1.76$ (weak-coupling regime), where k_B is the Boltzmann constant. The considered temperature is
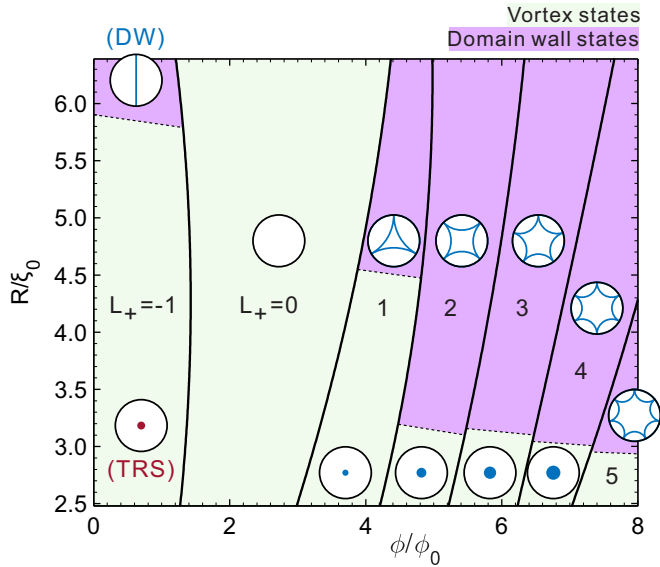
FIG. 1. The (magnetic flux, size) ground-state phase diagram for a mesoscopic p-wave disk. Magnetic flux ϕ through the sample is in units of flux quantum $\phi_0 = \frac{hc}{2e}$, and radius R of the sample is in units of BCS coherence length ξ_0. In small disks, the ground state is formed by (giant) composite vortex states with cylindrical symmetry, characterized by the sequentially increasing vorticity L_+. With increasing size the system undergoes symmetry-breaking phase transitions from composite vortex states to the chiral domain-wall states (except for the vortex-free state $L_+ = 0$). The number of chiral domain walls in a given state corresponds to $L_+ + 2$. Dashed lines indicate the second-order phase transitions and solid lines indicate the first-order ones.

$T = 0.1 T_c$, beyond the applicability range of the Ginzburg-Landau (GL) based models.

III. RESULTS

In this paper, we focus on small mesoscopic p-wave superconducting disks exposed to perpendicular magnetic field, to highlight the unique phase transitions in that regime. The ground state of the system is obtained by comparing the free-energy density G of all found states. The solutions are obtained by using different initial conditions for $\Delta_\pm(\mathbf{r})$, such as spatially randomized values (field-cooled conditions), different winding numbers, and/or different vortex configurations. We put forward our main results in Fig. 1, summarizing the equilibrium phase diagram as a function of the radius of the sample R, and the magnetic flux ϕ threading the sample.

Contrary to what many would expect, the ground state is not vortex free in absence of magnetic field. As seen in Fig. 1, the ground state at zero field is a vortex state with winding numbers $L_\pm = \mp 1$ in the two components of the order parameter. The vortex-free state, corresponding to the conventional Meissner state of s-wave superconductors, stabilizes as the ground state only at higher magnetic field.

We have actually checked that the ground state in the bulk sample with same parameters is the vortex-free state with $L_+ = 0$ ($L_- = L_+ + 2$ holds in all cases, and will be omitted from here on). Why is then the vortex state with $L_+ = -1$ the ground state at zero field for mesoscopic samples? To
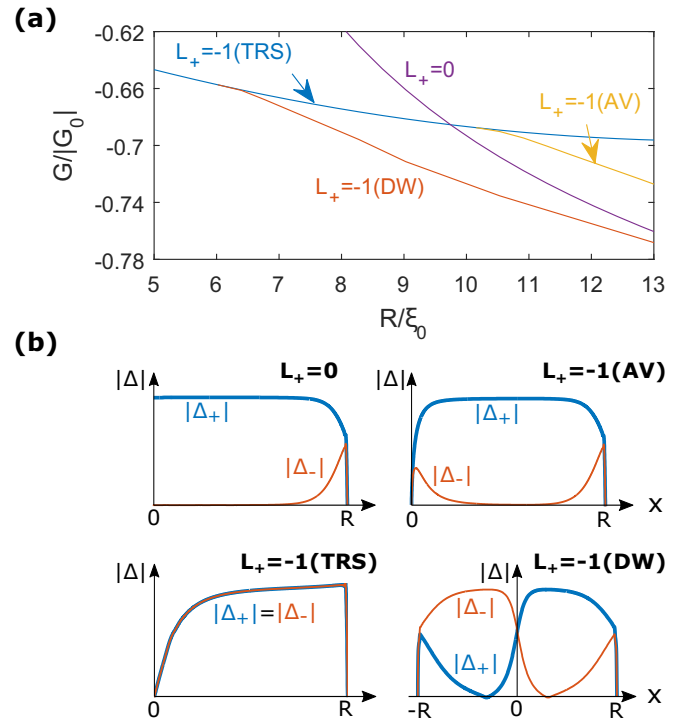
FIG. 2. (a) The superconducting free-energy density G of the superconducting states as a function of the sample size (R), in absence of magnetic field ($\phi = 0$). The $L_+ = -1$ domain wall (DW) state replaces the time-reversal-symmetric (TRS) $L_+ = -1$ vortex state as the ground state for $R \gtrsim 6\xi_0$. Note that the vortex-free state with $L_+ = 0$ becomes the ground state in much larger disks, while the antiparallel vortex state (AV) with $L_+ = -1$ (in which the Δ_- component is nearly completely suppressed) only exists as a metastable state. For clarity, the characteristic line profiles of the two components of the order parameter are shown in panel (b) for all aforementioned states.

explain this, we recall that chiral p-wave superconductors host edge states with an edge current [47,48] due to their topological nature. When decreasing the size of the sample (R), the edge states overlap and their interaction increases, causing destruction of superconductivity in the vicinity of the sample center, very similar to the normal vortex core. Due to this, as seen from Fig. 2, the Gibbs free-energy density of the vortex-free state with $L_+ = 0$ increases strongly with R decreasing. In contrast, the vortex state with $L_+ = -1$ in ultrasmall disks and at zero field exhibits lower energy, and preserves TRS. In this case, both components of the order parameter not only satisfy cylindrical symmetry, i.e., $\Delta_\pm = |\Delta_\pm(r)| e^{i L_\pm \theta}$, but also have the same spatial distribution, i.e., $|\Delta_+(r)| = |\Delta_-(r)|$. In other words, there is an antivortex at the center of the sample in one component, and a vortex at the very same place in the other component. Their supercurrents ideally cancel each other, making this phase stable at zero field. As a result, the $L_+ = -1$ (TRS) state is fostered by the interaction between the edge states, and the free energy of this state does not increase as fast as the energy of the vortex-free state with R decreasing. As seen from Fig. 2, the $L_+ = -1$ (TRS) state is the ground state in a wide range of small disks ($R \lesssim 6\xi_0$).
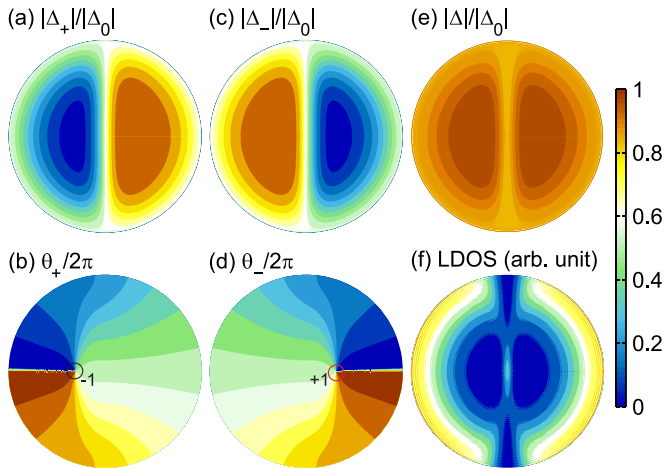
FIG. 3. Characterization of the $L_+ = -1$ domain-wall state. For the sample of size $R = 13\xi_0$ and zero magnetic field, we show the spatial distribution of the two components of the order parameter $|\Delta_\pm|$ (a), (c) and their phase $\theta_\pm$ (b), (d), respectively. Added circles in the phase plots mark the position of vortices (black/red circle for indicated negative/positive vorticity). Panel (e) shows the spatial distribution of the total order parameter $|\Delta| = \sqrt{|\Delta_+|^2 + |\Delta_-|^2}$ and (f) is the corresponding zero-bias LDOS.

Note that the so-called antiparallel vortex state [with $L_+ = -1$, but the nearly completely suppressed Δ_- component of the order parameter, thus labeled as $L_+ = -1$ (AV) from here on] does not exist in such a small disk. Although it stabilizes in larger samples, it remains metastable (i.e., with higher energy, as shown in Fig. 2), even for nonzero external magnetic field.

When the size of the sample R is increased, the confinement weakens. In this case, we find that in the $L_+ = -1$ (TRS) state the cores of the antivortex in Δ_+ and the vortex in Δ_- separate from each other, leading to broken cylindrical symmetry. As an illustrative example, we show the spatial profile of the order parameter after the formation of such a state in Figs. 3(a), 3(c) and 3(e). As seen there, Δ_+ and Δ_- segregate, and $|\Delta_+|$ becomes mirror symmetric with $|\Delta_-|$, as the antivortex shifts to the left side of the sample while the vortex shifts to the right side [see the plots of the phase of the respective components of the order parameter in Figs. 3(b) and 3(d)]. This results in a clear chiral domain wall between Δ_+ and Δ_-, passing through the center of the sample. The total order parameter, $|\Delta|$, is suppressed at the domain wall [shown in Fig. 3(e)]. In addition, as a topological defect, the domain wall carries low-lying bound states passing Fermi energy, leading to low-lying local-density-of-states (LDOS) distributions at the domain wall [23]. Figure 3(f) shows the zero-bias LDOS for the $L_+ = -1$ (DW) state in the sample with $R = 13\xi_0$. The domain wall yields a maximum in LDOS near the sample center. Near the sample edge, the domain wall causes suppression of the LDOS due to the interference effect between the domain-wall bound states and the edge bound states. The latter ones yield enhanced LDOS everywhere else near the sample edges. With increasing external magnetic field, the domain wall shifts to either left or right depending on the polarity of the applied field.
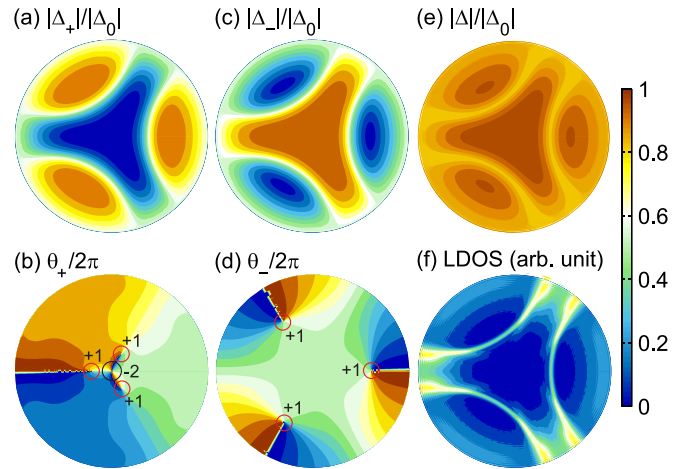
FIG. 4. Characterization of the $L_+ = 1$ domain-wall state (with three domain walls, as $L_- = 3$), for the sample with $R = 13\xi_0$ and $\phi = 4.8\phi_0$. Displayed quantities are the same as in Fig. 3. Added circles in the phase plots mark the position of vortices (black/red circle for indicated negative/positive vorticity).

The $L_+ = -1$ (DW) state replaces the $L_+ = -1$ (TRS) state as the ground state in larger samples, with radius beyond $\approx 6\xi_0$ [as seen in Fig. 2, the $L_+ = -1$ (DW) state attains lower free energy with respect to the $L_+ = -1$ (TRS) state for $R > 6\xi_0$]. The phase transition between $L_+ = -1$ (DW) and $L_+ = -1$ (TRS) states is of second order and therefore fully reversible, either as a function of size or as a function of applied magnetic field (corresponding to crossing the dashed line in Fig. 1).

Thus, to summarize the discussion so far, there are three stable states at zero field for a mesoscopic chiral p-wave superconductor, namely, (i) the $L_+ = -1$ (TRS) vortex state; (ii) the $L_+ = -1$ (DW) state, with one domain wall; and (iii) the $L_+ = 0$ vortex-free state. These states, respectively, replace one another in the ground state of the system, as the sample is made progressively larger.

With increasing magnetic field, we find a similar relationship between the vortex states and the domain-wall states for given vorticity. In the limit of very small samples, the composite (giant) vortex of successively increasing vorticity is the cylindrically symmetric ground state of the system, in agreement with previous Ginzburg-Landau investigations [39]. Note, however, that this behavior is not captured in Ref. [38], using a BdG formalism, where an erroneous phase diagram is presented. This being aside the main message of our present paper, we provide more details on the comparison of our results to those of Ref. [38] in Appendix B.

The main focus of our present paper is the topological phase transition occurring with increasing size of mesoscopic chiral p-wave superconductors, during which the two components of the order parameter segregate, and the composite vortex states are replaced by domain-wall states as the ground state of the system, for any applied magnetic field. For example, the vortex state with $L_+ = 1$ obeys cylindrical symmetry in ultrasmall samples ($R \lesssim 4.5\xi_0$), but develops into the three-domain-wall state in larger samples, shown in Fig. 4. More precisely, during this transition the giant vortex in Δ_- with winding number
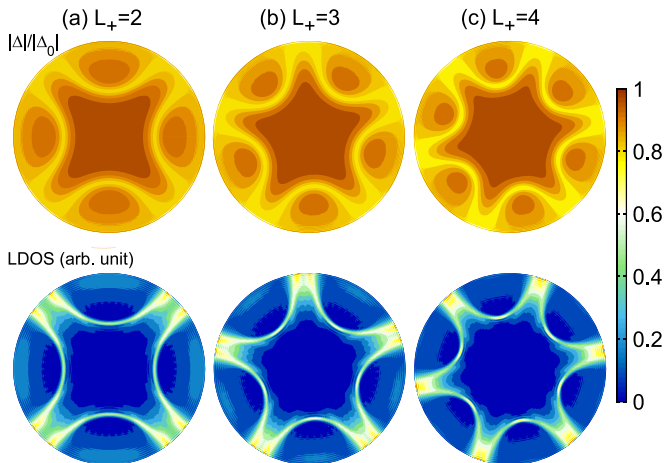
FIG. 5. The order-parameter distribution $|\Delta|$ (upper panels) and the corresponding zero-bias LDOS (lower panels) of the domain-wall states with $L_+ = 2$, 3, and 4 (respectively from left to right).

$L_- = 3$ splits into a multivortex state. Meanwhile, the vortex state in Δ_+ with $L_+ = 1$ hosts a vortex-antivortex molecule with net vorticity 1 (in order to best complement the symmetry of Δ_-, instead of a simple vortex, a giant antivortex with $L = -2$ is formed at the disk center surrounded by three vortices). At the domain walls, the total order parameter is depleted and the LDOS exhibits zero bias peaks.

To generalize our findings to all fields, the L_+ vorticity sequentially increases with applied magnetic field, and the number of domain walls for given L_+ vorticity matches $L_- = L_+ + 2$. Δ_+ consists of spread $L_+ + 2$ vortices and a centered giant antivortex with $L = -2$, while Δ_- consists of $L_+ + 2$ vortices. Spatial distributions of the order parameter (directly verifiable by, e.g., scanning tunneling microscopy) for states of higher vorticity are shown in Fig. 5, together with the corresponding zero-bias LDOS, all exhibiting low-lying states inside the domain walls. In the present paper we neglected the self-field of the superconductor, but it is trivial to conclude that the self-field of domain-wall states would be focused at the domain walls, offering a route for direct verification in magnetic-probe microscopy [49,50]. The range of sample sizes and the applied field needed for stability of each of the domain-wall states in the ground state is shown in Fig. 1. We note that the domain-wall states dominate the composite vortex states as magnetic field increases, i.e., the cylindrically symmetric states are not sufficient to describe the ground state at larger magnetic field even in very small p-wave samples.

As a last remark, we notice that the behavior of the zero-bias LDOS for the $L_+ = -1$ domain-wall state is different from the other domain-wall states at higher field [cf. Fig. 3(e) and lower panels of Fig. 5]. In the $L_+ = -1$ state, the domain wall suppresses the edge states in the sample, while the domain walls in higher-vorticity states enhance the LDOS peaks at the sample edge. This is due to the fact that in the $L_+ = -1$ state the domain wall separates a vortex in Δ_- and an antivortex in Δ_+, while in other states the domain wall separates vortices in both Δ_- and Δ_+. As a result, we identify two types of domain walls, exhibiting chirality-dependent effects on the edge states [51].

IV. CONCLUSIONS

In conclusion, motivated by recent experimental efforts, we reported the ground-state phase diagram in small-to-intermediate mesoscopic chiral p-wave superconducting samples exposed to perpendicular magnetic field. For this paper, we employed the self-consistent Bogoliubov–de Gennes numerical formalism, where we went beyond the approximations of similar earlier works. In ultrasmall samples, due to strong confinement, the ground states are the (giant) composite vortex states obeying cylindrical symmetry, in agreement with earlier results in literature [39] and conventional wisdom for small superconductors. However, in samples larger than few coherence lengths, the domain-wall states replace the vortex states as the ground state of the system. These domain walls mark the segregation of the two components of the order parameter and the vortices therein, and their number increases with increasing magnetic field. We also reveal two types of domain walls in a chiral p-wave superconductor, distinguished by their chirality-dependent effect on the edge states in the LDOS. These domain walls can be directly visualized by scanning tunneling microscopy as locally suppressed order parameter and correspondingly boosted bound states in the LDOS, or by magnetic-probe microscopy as locally focused self-field of the sample. These predictions are relevant to recent realizations of two-dimensional topological superconductivity in the mesoscopic limit, as in, for example, atomically thin Pb/Co on Si(111), where the size of the p-wave system can be adjusted by the size of the underlying Co cluster [44], but one chirality of the order parameter is favored with respect to the other by spin-orbit coupling and the s-wave component is also present. On theoretical grounds, our results translate to other superconducting systems with a multicomponent order parameter (e.g., $d + id$ systems [20] or chiral multiband ones [52,53]), where similar topological transitions from overlapping to segregated components can be expected and emergent physics can be significantly richer than in standard single-component superconductors.

APPENDIX A: THE FREE ENERGY

In this Appendix, we derive the expression of the Gibbs free energy for the chiral p-wave superconducting state. Throughout the derivation, the Cartesian system of coordinates is used. Subsequently, we apply the obtained expression for the free energy to the homogeneous system as a quick check of the validity of our approach.

1. Derivation of the free-energy equation

The BdG equations for a chiral spin-triplet p-wave superconductor [54], with the order parameter described by the

vector $\vec{d}(\vec{k}) = \hat{z}\frac{\Delta}{k_F}(k_x \pm ik_y)$, are written as

$$\begin{bmatrix} H_e & \Pi(\mathbf{r}) \\ -\Pi^*(\mathbf{r}) & -H_e^* \end{bmatrix} \begin{bmatrix} u_n(\mathbf{r}) \\ v_n(\mathbf{r}) \end{bmatrix} = E_n \begin{bmatrix} u_n(\mathbf{r}) \\ v_n(\mathbf{r}) \end{bmatrix}, \qquad (A1)$$

where

$$H_e = \frac{1}{2m}\left(\frac{\hbar}{i}\nabla - \frac{e}{c}\mathbf{A}\right)^2 - E_F \qquad (A2)$$

is the single-particle Hamiltonian, with E_F the Fermi energy and $\mathbf{A}$ the vector potential. Term $\Pi(\mathbf{r})$ is written as

$$\Pi(\mathbf{r}) = -\frac{i}{k_F}\left\{ \Delta_x(\mathbf{r})\frac{\partial}{\partial x} + i\Delta_y(\mathbf{r})\frac{\partial}{\partial y} \right.$$
$$\left. + \frac{1}{2}\left[\frac{\partial \Delta_x(\mathbf{r})}{\partial x} + i\frac{\partial \Delta_y(\mathbf{r})}{\partial y}\right] \right\}, \qquad (A3)$$

where $\Delta_x(\mathbf{r})$ and $\Delta_y(\mathbf{r})$ are p_x and p_y components of the order parameter, respectively, $u_n(v_n)$ are electron(hole)-like quasiparticle eigen-wave-functions, and E_n are the corresponding quasiparticle eigenenergies. The transformation from Δ_x and Δ_y to $\Delta_\pm$ is made by $\Delta_x = \Delta_+ + \Delta_-$ and $\Delta_y = \Delta_+ - \Delta_-$. In addition, the self-consistent gap equations are

$$\Delta_x(\mathbf{r}) = -i\frac{g}{k_F}\sum_{E_n < \hbar\omega_D}\left[v_n^*(\mathbf{r})\frac{\partial u_n(\mathbf{r})}{\partial x} - u_n(\mathbf{r})\frac{\partial v_n^*(\mathbf{r})}{\partial x}\right]$$
$$\times [1 - 2f(E_n)],$$
$$\Delta_y(\mathbf{r}) = -\frac{g}{k_F}\sum_{E_n < \hbar\omega_D}\left[v_n^*(\mathbf{r})\frac{\partial u_n(\mathbf{r})}{\partial y} - u_n(\mathbf{r})\frac{\partial v_n^*(\mathbf{r})}{\partial y}\right]$$
$$\times [1 - 2f(E_n)], \qquad (A4)$$

where $f(E_n)$ is the Fermi distribution function. The summations in Eqs. (A4) are over all the quasiparticle states with energies in the Debye window $\hbar\omega_D$.

Next, we derive the Gibbs free energy for a p-wave superconductor, first written as

$$\mathcal{G} = \langle H_{\text{eff}} \rangle - TS + F_H, \qquad (A5)$$

where $F_H = (\mathbf{B} - \mathbf{H})^2/8\pi$ is the magnetic energy, TS is the energy induced by entropy, and $\langle H_{\text{eff}} \rangle$ is the expectation value of the effective Hamiltonian. According to Ref. [55], the effective Hamiltonian for an unconventional superconductor is written as

$$\langle H_{\text{eff}} \rangle = \underbrace{\int d\mathbf{r} \int d\mathbf{r}' \sum_\sigma \left[\Psi^\dagger(\mathbf{r}\sigma)\hat{H}_e \delta(\mathbf{r} - \mathbf{r}')\Psi(\mathbf{r}'\sigma)\right]}_{\langle H_e \rangle}$$
$$+ \underbrace{\int d\mathbf{r} \int d\mathbf{r}' \Delta(\mathbf{r},\mathbf{r}')\Psi^\dagger(\mathbf{r}\uparrow)\Psi^\dagger(\mathbf{r}'\downarrow)}_{\langle \Delta \rangle}$$
$$+ \underbrace{\int d\mathbf{r} \int d\mathbf{r}' \Delta^*(\mathbf{r},\mathbf{r}')\Psi(\mathbf{r}'\downarrow)\Psi(\mathbf{r}\uparrow)}_{\langle \Delta^* \rangle}$$
$$+ \underbrace{\int d\mathbf{r} \int d\mathbf{r}' W(\mathbf{r},\mathbf{r}')}_{\langle W \rangle}, \qquad (A6)$$

where

$$W(\mathbf{r},\mathbf{r}') = \hat{V}(\mathbf{r},\mathbf{r}')\langle\Psi^\dagger(\mathbf{r},\uparrow)\Psi^\dagger(\mathbf{r}',\downarrow)\rangle\langle\Psi(\mathbf{r}',\downarrow)\Psi(\mathbf{r},\uparrow)\rangle \qquad (A7)$$

is a constant term in the mean-field theory needed to match the expectation value of the mean-field Hamiltonian with the one of the many-body Hamiltonian. For p-wave pairing [45], the spatial dependence of the order parameter can be written as

$$\Delta(\mathbf{r},\mathbf{r}') = \frac{i}{k_F}[\Delta_x(\mathbf{R})\partial_{x'} + i\Delta_y(\mathbf{R})\partial_{y'}]\delta(\mathbf{r} - \mathbf{r}'), \qquad (A8)$$

with $\mathbf{R} = (\mathbf{r} + \mathbf{r}')/2$.

Next, we calculate the first term in Eq. (A6), $\langle H_e \rangle$. First, we introduce the Bogoliubov transformations:

$$\Psi^\dagger(\mathbf{r},\uparrow) = \sum_n (u_n^*(\mathbf{r})\gamma_{n\uparrow}^\dagger + v_n(\mathbf{r})\gamma_{n\downarrow}),$$
$$\Psi(\mathbf{r},\downarrow) = \sum_n (v_n^*(\mathbf{r})\gamma_{n\uparrow}^\dagger + u_n(\mathbf{r})\gamma_{n\downarrow}). \qquad (A9)$$

Note that these are slightly different from those used for s-wave pairing. The thermal averages of the fermionic γ operators are as usual

$$\langle\gamma_{n\sigma}^\dagger\gamma_{n'\sigma'}\rangle = \delta_{\sigma\sigma'}\delta_{nn'}f(E_n),$$
$$\langle\gamma_{n\sigma}\gamma_{n'\sigma'}^\dagger\rangle = \delta_{\sigma\sigma'}\delta_{nn'}[1 - f(E_n)], \qquad (A10)$$
$$\langle\gamma_{n\sigma}\gamma_{n'\sigma'}\rangle = \langle\gamma_{n\sigma}^\dagger\gamma_{n'\sigma'}^\dagger\rangle = 0.$$

Substituting Eqs. (A9) and (A10) into $\langle H_e \rangle$, we obtain

$$\langle H_e \rangle = 2\int d\mathbf{r} \sum_n [u_n^*\hat{H}_e u_n f_n + v_n\hat{H}_e v_n^*(1 - f_n)]. \qquad (A11)$$

The factor of 2 is due to the two spin orientations in the electron and the hole sectors. Substituting Eq. (A1) into Eq. (A11) yields

$$\langle H_e \rangle = 2\int d\mathbf{r} \sum_n \{E_n|u_n|^2 f_n - E_n|v_n|^2(1 - f_n)$$
$$- u_n^*\Pi(\mathbf{r})v_n f_n - v_n\Pi(\mathbf{r})u_n^*(1 - f_n)\}. \qquad (A12)$$

Here Π is calculated using Eq. (A3) with the initial input of Δ_x and Δ_y.

Next, we calculate the second term $\langle \Delta \rangle$ in Eq. (A6). Substituting Eqs. (A9) and (A10) into it, we obtain

$$\langle \Delta \rangle = \int d\mathbf{r} \int d\mathbf{r}'\Delta(\mathbf{r},\mathbf{r}')[u_n^*(\mathbf{r})v_n(\mathbf{r}')f_n$$
$$+ v_n(\mathbf{r})u_n^*(\mathbf{r}')(1 - f_n)]. \qquad (A13)$$

Substituting Eq. (A8) into Eq. (A13) and integrating by parts yields

$$\langle \Delta \rangle = \int d\mathbf{r} \sum_n \{u_n^*\Pi'(\mathbf{r})v_n f_n + v_n\Pi'(\mathbf{r})u_n^*(1 - f_n)\}. \qquad (A14)$$

Here Π' indicates that Δ_x and Δ_y are calculated from Eq. (A4) using the quasiparticle states. Similarly, the third term in Eq. (A6) becomes $\langle \Delta^* \rangle = \langle \Delta \rangle$ and the last term $\langle W \rangle = -\langle \Delta \rangle$. In the calculation of the $\langle W \rangle$ term we used the definition of the order parameter, $\Delta(\mathbf{r},\mathbf{r}') = \hat{V}(\mathbf{r},\mathbf{r}')\langle\Psi(\mathbf{r}',\uparrow)\Psi(\mathbf{r}',\downarrow)\rangle$.

Finally, the Gibbs free energy is written as

$$
\begin{aligned}
\mathcal{G} &= \langle H_{\text{eff}} \rangle - TS + F_H \\
&= \sum_n \left\{ 2E_n f_n - 2E_n \int d\mathbf{r} |v_n|^2 - 2 \int d\mathbf{r} [u_n^* \Pi(\mathbf{r}) v_n f_n + v_n \Pi(\mathbf{r}) u_n^* (1 - f_n)] \right. \\
&\quad \left. + \int d\mathbf{r} [u_n^* \Pi'(\mathbf{r}) v_n f_n + v_n \Pi'(\mathbf{r}) u_n^* (1 - f_n)] \right\} - TS + F_H.
\end{aligned}
\tag{A15}
$$

When the converged Δ_x and Δ_y are reached, then $\Pi = \Pi'$ and the Gibbs free energy shown in Eq. (A15) will be further reduced to

$$
\mathcal{G} = \sum_n \left\{ 2E_n f_n - 2E_n \int d\mathbf{r} |v_n|^2 - \int d\mathbf{r} [u_n^* \Pi(\mathbf{r}) v_n f_n + v_n \Pi(\mathbf{r}) u_n^* (1 - f_n)] \right\} - TS + F_H.
\tag{A16}
$$

This is the expression we used in the present paper. The summation is done over the entire spectrum. Note that there are *no assumptions made* on the energy range of the pairing potential $V(r,r')$, therefore this expression is valid irrespectively of the relation between Δ and $\hbar \omega_D$. In the weak-coupling BCS limit, i.e., for $\Delta \ll \hbar \omega_D \ll E_F$, and for s-wave pairing, this expression reduces to the well-known expression

$$
\begin{aligned}
\mathcal{G} &= \sum_n \left(2E_n f_n - 2E_n \int d\mathbf{r} |v_n|^2 \right) \\
&\quad + \int d\mathbf{r} \frac{|\Delta|^2}{g} - TS + F_H,
\end{aligned}
\tag{A17}
$$

which is another proof of the consistency of our derivation.

2. Free energy of the homogeneous system

In this subsection, we present the form of the equations in the homogeneous case in order to show that our free energy is correct. If the expression of the free energy is valid, the calculated energy should always decrease during the self-consistent procedure since the order parameter approaches its true (lowest) equilibrium value.

For the homogeneous case (two-dimensional), we consider a square unit cell of length W. The components of the order parameter are constant, i.e., $\Delta_x(\mathbf{r}) = \Delta_x$ and $\Delta_y(\mathbf{r}) = \Delta_y$. $u_n(\mathbf{r})$ and $v_n(\mathbf{r})$ can be expanded in terms of plane waves, i.e., as

$$
\begin{pmatrix} u_n(\mathbf{r}) \\ v_n(\mathbf{r}) \end{pmatrix} = \sum_{\mathbf{k}} \frac{e^{i\mathbf{k} \cdot \mathbf{r}}}{W} \begin{pmatrix} u_{\mathbf{k}} \\ v_{\mathbf{k}} \end{pmatrix},
\tag{A18}
$$

where $\mathbf{k} = (k_x, k_y) = 2\pi(j_x, j_y)/W$ is the momentum, given that $j_x, j_y \in \mathbb{Z}$. In the absence of the magnetic field, $\mathbf{k}$ is a good quantum number and the BdG equations (A1) for a given $\mathbf{k}$ are written as

$$
\begin{bmatrix} \epsilon_{\mathbf{k}} & \Pi_{\mathbf{k}} \\ \Pi_{\mathbf{k}}^* & -\epsilon_{\mathbf{k}} \end{bmatrix} \begin{bmatrix} u_{\mathbf{k}} \\ v_{\mathbf{k}} \end{bmatrix} = E_{\mathbf{k}} \begin{bmatrix} u_{\mathbf{k}} \\ v_{\mathbf{k}} \end{bmatrix},
\tag{A19}
$$

where $\epsilon_{\mathbf{k}} = \hbar^2 \mathbf{k}^2/2m - E_F$ and $\Pi_{\mathbf{k}} = (k_x \Delta_x + i k_y \Delta_y)/k_F$. We take the basis functions the $\epsilon_{\mathbf{k}}$ of which satisfy $|\epsilon_{\mathbf{k}}| < \hbar \omega_D$.

Then, the self-consistent gap equations (A4) are

$$
\begin{aligned}
\Delta_x &= \frac{2g}{k_F} \sum_{\substack{\mathbf{k} \\ E_{\mathbf{k}} < \hbar \omega_D}} k_x u_{\mathbf{k}} v_{\mathbf{k}}^* [1 - 2f(E_{\mathbf{k}})], \\
\Delta_y &= -i \frac{2g}{k_F} \sum_{\substack{\mathbf{k} \\ E_{\mathbf{k}} < \hbar \omega_D}} k_y u_{\mathbf{k}} v_{\mathbf{k}}^* [1 - 2f(E_{\mathbf{k}})].
\end{aligned}
\tag{A20}
$$

From Eq. (A15), the Gibbs free energy is

$$
\begin{aligned}
\mathcal{G} &= \sum_{\mathbf{k}} (2E_{\mathbf{k}} f(E_{\mathbf{k}}) - 2E_{\mathbf{k}} |v_{\mathbf{k}}|^2 - \{u_{\mathbf{k}}^* (2\Pi_{\mathbf{k}} - \Pi_{\mathbf{k}}') v_{\mathbf{k}} f(E_{\mathbf{k}}) \\
&\quad + v_{\mathbf{k}} (2\Pi_{\mathbf{k}} - \Pi_{\mathbf{k}}') u_{\mathbf{k}}^* [1 - f(E_{\mathbf{k}})]\}) - TS.
\end{aligned}
\tag{A21}
$$

The superconducting free-energy density G is given according to Eq. (10).

Next, we present results for parameters as those used in Ref. [38]. $W = 1\,\mu\text{m}$ is sufficiently large so that results will not change for further enlarged W. Figures 6(a) and 6(b) show the calculated order parameter and the corresponding free energy, respectively, as a function of iteration steps at $T = 0\,\text{K}$. During the iterations, we find that two components of the order parameter are always the same, i.e., $\Delta_x = \Delta_y = \Delta$. Δ converges to 0.22 meV, which results in the zero-temperature coherence length $\xi_0 \approx 72\,\text{nm}$ ($\xi_0 = \hbar v_F/\pi \Delta_0$, with Fermi velocity $v_F = \sqrt{2E_F/m_e}$, Fermi energy $E_F = 16.32\,\text{meV}$, and zero-temperature order parameter $\Delta_0 = 0.22\,\text{meV}$) and the critical temperature $T_{c,\text{bulk}} \approx 1.5\,\text{K}$. The free energy shown
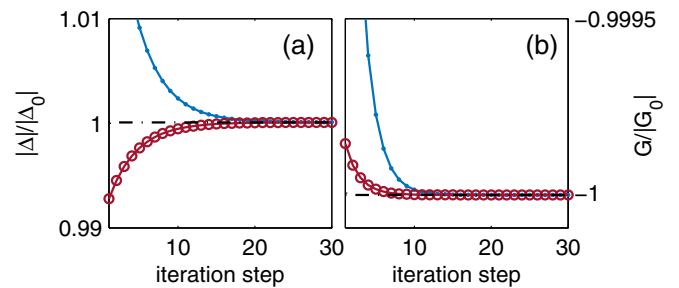
FIG. 6. (a) The order parameter Δ_x (which equals Δ_y in this simulation) and (b) the superconducting free-energy density G, as a function of the iteration step. The solid line corresponds to the case of initial order parameter larger than the converged value, while the line with open dots corresponds to the initial order parameter smaller than the converged value. For both cases the free energy decreases with the iterations, and the final values are the same.

in Fig. 6(b) always decreases with the iterations and yields the same result, irrespectively of the initial amplitude of the order parameter being larger or smaller than the converged value. These results prove the reliability of our free-energy calculation. These hold in all cases including in the mesoscopic samples.

Note that the Gibbs free energy from Eq. (A21) for converged order parameters can be written as

$$\mathcal{G} = \sum_{\mathbf{k}} \{2E_{\mathbf{k}} f(E_{\mathbf{k}}) - 2E_{\mathbf{k}}|v_{\mathbf{k}}|^2$$
$$+ \Pi_{\mathbf{k}} u_{\mathbf{k}}^* v_{\mathbf{k}} [1 - 2f(E_{\mathbf{k}})]\} - TS. \quad (A22)$$

We find that

$$\sum_{\mathbf{k}} \Pi_{\mathbf{k}} u_{\mathbf{k}}^* v_{\mathbf{k}} [1 - 2f(E_{\mathbf{k}})] = \frac{|\Delta_x|^2 + |\Delta_y|^2}{2g} W^2, \quad (A23)$$

given that all the $\mathbf{k}$ states have the same coupling constant g. Factor W^2 is due to the area of the unit cell. Finally, in the homogeneous case the Gibbs free energy can be written as

$$\mathcal{G} = \sum_{\mathbf{k}} 2E_{\mathbf{k}} f(E_{\mathbf{k}}) - 2E_{\mathbf{k}}|v_{\mathbf{k}}|^2 + \frac{|\Delta_x|^2 + |\Delta_y|^2}{2g} W^2 - TS. \quad (A24)$$

APPENDIX B: COMPARISON WITH OTHER AVAILABLE RESULTS IN THE LITERATURE

In this Appendix, we discuss in more detail the bottom part of the phase diagram presented in Fig. 1, where only cylindrically symmetric states are found, in a sequence corresponding to increasing vorticity (from $L_+ = -1$ to 5). This is needed since earlier calculations of Ref. [38] reported a rather different phase diagram from ours. Namely, in those calculations, in very small disks in absence of magnetic field the ground state was either a normal state or a $L_+ = 0$ state, and the $L_+ = -1$ state was induced in the system by larger magnetic field.

In what follows, we revisit the BdG numerical simulations of Ref. [38] for mesoscopic disks and find that the main claim of their work, i.e., the existence of a field-induced state with winding number $L_+ = -1$ in mesoscopic p-wave superconductors, is incorrect. We performed the same type of calculation, under the same conditions, but did not find any signature of the reported behavior. We instead find that the phase diagram with respect to field and temperature is a more conventional one, in agreement with GL simulations of Ref. [39].

The taken parameters, same as used in Ref. [38], have been introduced in Sec. II. First, we show in Fig. 7 the components $\Delta_\pm(r)$ and the supercurrent density $j_\theta(r)$ for states $L_+ = -1$ and 0. The results for disks with small radii are quite different from those for large radii presented in Fig. 2 of Ref. [38]. As shown in Figs. 7(a) and 7(c), the $L_+ = -1$ state is time-reversal symmetric due to boundary effects. As a result, the current is zero in the absence of the magnetic field, which makes the state more stable when $\phi = 0$, where ϕ is the magnetic flux through the sample. We recover the radial dependence of the supercurrent presented in Ref. [38] only for $R > 10\xi_0$, but, as shown in the main body of this
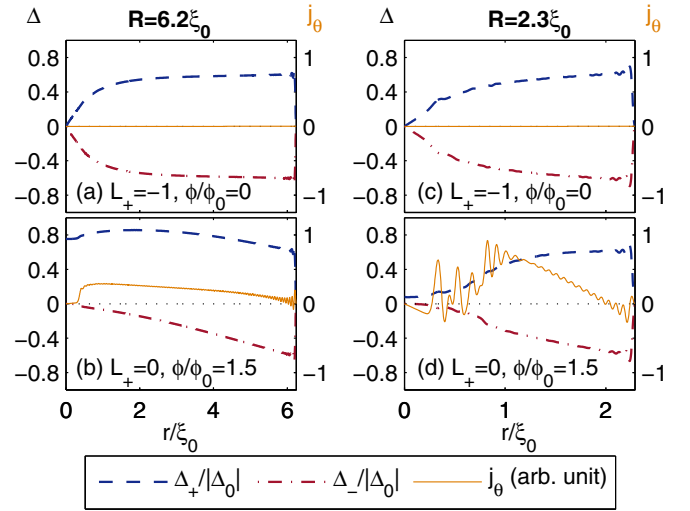
FIG. 7. Spatial distribution of the order-parameter components $\Delta_\pm(r)$ and the supercurrent density $j_\theta(r)$, for enforced cylindrical symmetry, in the sample with radius $R = 6.2\xi_0$ for $L_+ = -1$ (a) and $L_+ = 0$ (b), and for the sample with radius $R = 2.3\xi_0$ for $L_+ = -1$ (c) and $L_+ = 0$ (d).

paper, for those sizes of the sample the cylindrical symmetry of the superconducting state no longer holds. The $L_+ = 0$ state [shown in Figs. 7(b) and 7(d)] has a broken time-reversal symmetry, with spontaneous chiral edge currents. However, the current exhibits sudden changes near the center of the sample due to the competition between the surface current and the cylindrical symmetry. When $R = 2.3\xi_0$, as shown in Fig. 7(d), this competition, together with the increased importance of quantum confinement, induces oscillations in j_θ on the scale of $1/k_F$, while also enhancing it. Δ_+ is therefore weakened near the center, signaling that the $L_+ = 0$ state becomes less favorable in small samples.

In Fig. 8, we show the calculated dependence of the spatially averaged order parameter $\bar{\Delta}$ for states $L_+ = -1$ and 0 on the sample size and temperature. This dependence is similar to the results shown in Figs. 3(a) and 3(b) in Ref. [38]. However, the quantum size effect is robust when $R \sim 1/k_F$, which results in oscillations in $\bar{\Delta}(R)$. These were not shown in Ref. [38].

Once the self-consistent result is reached, the Gibbs free energy is calculated using Eq. (A16). The superconducting
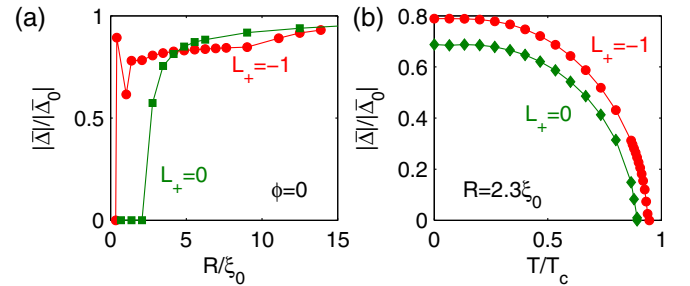
FIG. 8. (a) Spatially averaged order parameter $\bar{\Delta} = \sqrt{|\Delta_+|^2 + |\Delta_-|^2}$ as a function of the sample radius R at $\phi = 0$ and $T = 0$, for the states $L_+ = -1$ and 0. (b) $\bar{\Delta}$ as a function of T for sample radius $R = 2.3\xi_0$ for $L_+ = -1$ at $\phi = 0$ and for $L_+ = 0$ at $\phi = 1.5\phi_0$.
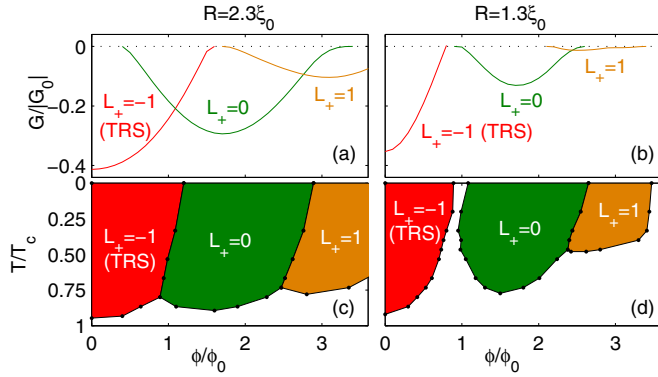
FIG. 9. Free-energy density G of the superconducting states as a function of magnetic flux threading the sample, ϕ, for a p-wave mesoscopic disk of radius (a) $R = 2.3\xi_0$ and (b) $R = 1.3\xi_0$ at $T = 0.33 T_c$. The corresponding $\phi - T$ equilibrium phase diagrams are shown in (c) and (d), respectively (cf. the erroneous Figs. 3(c) and 3(d) of Ref. [38]).

free-energy density G, for radii $R = 2.3\xi_0$ and $1.3\xi_0$, is shown as a function of ϕ in Fig. 9. These results agree with conventional wisdom and are similar to those for mesoscopic s-wave superconductors obtained by the GL theory in, e.g., Ref. [31]. $G(\phi)$ plots were not presented in Ref. [38], and therefore one has no means to directly validate their $\phi - T$ phase diagram.

From Figs. 9(a) and 9(b) it is clear that at low fields and for the considered dimensions of the sample the ground state is always the $L_+ = -1$ state. As the field is increased, a first-order phase transition to the $L_+ = 0$ state takes place. By decreasing the size of the system, the $L_+ = -1$ state becomes

more stable while the phase boundary between the two states moves to lower fields. If the size is decreased even further, the $L_+ = -1$ and 0 superconducting states become separated by the normal state. This finite-size reentrant effect is similar to already observed oscillations of the critical temperature in s-wave superconducting rings [56]. This is not surprising since in the small radius limit both Δ_+ and Δ_- components of the order parameter are strongly suppressed in the center of the disk, effectively mimicking a superconducting ring.

Finally, we present in Figs. 9(c) and 9(d) the correct ground-state $\phi - T$ phase diagrams for samples with radius $R = 2.3\xi_0$ and $1.3\xi_0$. The results are physically understandable, as states always appear sequentially in the winding number of the dominant $p_x + i p_y$ component as ϕ increases. Moreover, our results at finite temperature are consistent with those shown in Ref. [39], where a Ginzburg-Landau simulation was performed for a similar system.

To conclude, we find that the phase diagram of Ref. [38] is incorrect. To substantiate our conclusion we performed identical BdG calculations for a disk geometry and showed explicitly the correct form of the free energy based on which the equilibrium phase diagram is constructed. Our free-energy versus magnetic-field curves provide a clear picture of the nature of the ground state, which at zero field is always the $L_+ = -1$ state (in the range of parameters of interest here, i.e., for small samples). Additional support to our claims comes from the calculations performed in Ref. [39] within the GL model, which delivered a very similar phase diagram to ours. Finally, we note again that this discussion is related only to the limit of very small samples, whereas the focus of our present paper is on novel states in *larger* mesoscopic p-wave samples where cylindrical symmetry is *broken*, leading to a much richer phase diagram.

[1] Y. Tanaka, Multicomponent superconductivity based on multiband superconductors, Supercond. Sci. Technol. **28**, 034002 (2015).

[2] S.-Z. Lin, Ground state, collective mode, phase soliton and vortex in multiband superconductors, J. Phys.: Condens. Matter **26**, 493202 (2014).

[3] M. V. Milošević and A. Perali, Emergent phenomena in multicomponent superconductivity: An introduction to the focus issue, Supercond. Sci. Technol. **28**, 060201 (2015).

[4] S.-Z. Lin and X. Hu, Massless Leggett Mode in Three-Band Superconductors with Time-Reversal-Symmetry Breaking, Phys. Rev. Lett. **108**, 177005 (2012).

[5] E. Babaev, Vortices with Fractional Flux in Two-Gap Superconductors and in Extended Faddeev Model, Phys. Rev. Lett. **89**, 067001 (2002).

[6] E. Babaev, L. D. Faddeev, and A. J. Niemi, Hidden symmetry and knot solitons in a charged two-condensate Bose system, Phys. Rev. B **65**, 100512 (2002).

[7] Y. Tanaka, Soliton in Two-Band Superconductor, Phys. Rev. Lett. **88**, 017002 (2001).

[8] S.-Z. Lin and X. Hu, Phase solitons in multi-band superconductors with and without time-reversal symmetry, New J. Phys. **14**, 063021 (2012).

[9] L. Komendová, Y. Chen, A. A. Shanenko, M. V. Milošević, and F. M. Peeters, Two-Band Superconductors: Hidden Criticality Deep in the Superconducting State, Phys. Rev. Lett. **108**, 207002 (2012).

[10] C. Kallin, Chiral p-wave order in Sr_2RuO_4, Rep. Prog. Phys. **75**, 042501 (2012).

[11] C. Kallin and J. Berlinsky, Chiral superconductors, Rep. Prog. Phys. **79**, 054502 (2016).

[12] G. E. Volovik, *The Universe in a Helium Droplet*, 1st ed. (Oxford University, Oxford, 2009).

[13] Y. Maeno, H. Hashimoto, K. Yoshida, S. Nishizaki, T. Fujita, J. G. Bednorz, and F. Lichtenberg, Superconductivity in a layered perovskite without copper, Nature (London) **372**, 532 (1994).

[14] M. Matsumoto and M. Sigrist, Chiral optical absorption by a vortex in $p_x \pm i p_y$-wave superconductor, J. Phys. Soc. Jpn. **68**, 724 (1999).

[15] J. A. Sauls and M. Eschrig, Vortices in chiral, spin-triplet superconductors and superfluids, New J. Phys. **11**, 075008 (2009).

[16] T. Yokoyama, C. Iniotakis, Y. Tanaka, and M. Sigrist, Chirality Sensitive Effect on Surface States in Chiral p-Wave Superconductors, Phys. Rev. Lett. **100**, 177002 (2008).

[17] M. Matsumoto and M. Sigrist, Quasiparticle states near the surface and the domain wall in a $p_x \pm ip_y$-wave superconductor, J. Phys. Soc. Jpn. **68**, 994 (1999).

[18] I. Serban, B. Béri, A. R. Akhmerov, and C. W. J. Beenakker, Domain Wall in a Chiral *p*-Wave Superconductor: A Pathway for Electrical Current, Phys. Rev. Lett. **104**, 147001 (2010).

[19] V. F. Becerra and M. V. Milošević, Multichiral ground states in mesoscopic *p*-wave superconductors, Phys. Rev. B **94**, 184517 (2016).

[20] O. A. Awoga, A. Bouhon, and A. M. Black-Schaffer, Domain walls in a chiral *d*-wave superconductor on the honeycomb lattice, Phys. Rev. B **96**, 014521 (2017).

[21] J. Garaud and E. Babaev, Skyrmionic state and stable half-quantum vortices in chiral *p*-wave superconductors, Phys. Rev. B **86**, 060514 (2012).

[22] V. F. Becerra, E. Sardella, F. M. Peeters, and M. V. Milošević, Vortical versus skyrmionic states in mesoscopic *p*-wave superconductors, Phys. Rev. B **93**, 014518 (2016).

[23] L.-F. Zhang, V. F. Becerra, L. Covaci, and M. V. Milošević, Electronic properties of emergent topological defects in chiral *p*-wave superconductivity, Phys. Rev. B **94**, 024520 (2016).

[24] J. Garaud and E. Babaev, Properties of skyrmions and multi-quanta vortices in chiral *p*-wave superconductors, Sci. Rep. **5**, 17540 (2015).

[25] N. Read and D. Green, Paired states of fermions in two dimensions with breaking of parity and time-reversal symmetries and the fractional quantum Hall effect, Phys. Rev. B **61**, 10267 (2000).

[26] X.-L. Qi and S.-C. Zhang, Topological insulators and superconductors, Rev. Mod. Phys. **83**, 1057 (2011).

[27] D. A. Ivanov, Non-Abelian Statistics of Half-Quantum Vortices in *p*-Wave Superconductors, Phys. Rev. Lett. **86**, 268 (2001).

[28] J. Jang, D. G. Ferguson, V. Vakaryuk, R. Budakian, S. B. Chung, P. M. Goldbart, and Y. Maeno, Observation of half-height magnetization steps in Sr_2RuO_4, Science **331**, 186 (2011).

[29] S. Autti, V. V. Dmitriev, J. T. Mäkinen, A. A. Soldatov, G. E. Volovik, A. N. Yudin, V. V. Zavjalov, and V. B. Eltsov, Observation of Half-Quantum Vortices in Topological Superfluid ^{3}He, Phys. Rev. Lett. **117**, 255301 (2016).

[30] A. K. Geim, I. V. Grigorieva, S. V. Dubonos, J. G. S. Lok, J. C. Maan, A. E. Filippov, and F. M. Peeters, Phase transitions in individual sub-micrometre superconductors, Nature (London) **390**, 259 (1997).

[31] V. A. Schweigert, F. M. Peeters, and P. S. Deo, Vortex Phase Diagram for Mesoscopic Superconducting Disks, Phys. Rev. Lett. **81**, 2783 (1998).

[32] B. Xu, M. V. Milošević, and F. M. Peeters, Magnetic properties of vortex states in spherical superconductors, Phys. Rev. B **77**, 144509 (2008).

[33] G. R. Berdiyorov, A. D. Hernandez, and F. M. Peeters, Confinement Effects on Intermediate-State Flux Patterns in Mesoscopic type-I Superconductors, Phys. Rev. Lett. **103**, 267002 (2009).

[34] L.-F. Zhang, L. Covaci, M. V. Milošević, G. R. Berdiyorov, and F. M. Peeters, Unconventional Vortex States in Nanoscale Superconductors due to Shape-Induced Resonances in the Inhomogeneous Cooper-Pair Condensate, Phys. Rev. Lett. **109**, 107001 (2012); Vortex states in nanoscale superconducting squares: The influence of quantum confinement, Phys. Rev. B **88**, 144501 (2013).

[35] A. Kanda, B. J. Baelus, F. M. Peeters, K. Kadowaki, and Y. Ootuka, Experimental Evidence for Giant Vortex States in a Mesoscopic Superconducting Disk, Phys. Rev. Lett. **93**, 257002 (2004).

[36] T. Cren, L. Serrier-Garcia, F. Debontridder, and D. Roditchev, Vortex Fusion and Giant Vortex States in Confined Superconducting Condensates, Phys. Rev. Lett. **107**, 097202 (2011).

[37] L. F. Chibotaru, V. H. Dao, and A. Ceulemans, Thermodynamically stable noncomposite vortices in mesoscopic two-gap superconductors, Europhys. Lett. **78**, 47001 (2007).

[38] J.-W. Huo, W.-Q. Chen, S. Raghu, and F.-C. Zhang, Field-Induced *p*-Wave Superconducting State of Mesoscopic Systems, Phys. Rev. Lett. **108**, 257002 (2012).

[39] B.-L. Huang and S.-K. Yip, Phase diagrams of a *p*-wave superconductor inside a mesoscopic disk-shaped sample, Phys. Rev. B **86**, 064506 (2012).

[40] L. Fu and C. L. Kane, Superconducting Proximity Effect and Majorana Fermions at the Surface of a Topological Insulator, Phys. Rev. Lett. **100**, 096407 (2008).

[41] V. Mourik, K. Zuo, S. M. Frolov, S. R. Plissard, E. P. A. M. Bakkers, and L. P. Kouwenhoven, Signatures of majorana fermions in hybrid superconductor-semiconductor nanowire devices, Science **336**, 1003 (2012).

[42] J. D. Sau, R. M. Lutchyn, S. Tewari, and S. Das Sarma, Generic New Platform for Topological Quantum Computation using Semiconductor Heterostructures, Phys. Rev. Lett. **104**, 040502 (2010).

[43] A. D. Bernardo, O. Millo, M. Barbone, H. Alpern, Y. Kalcheim, U. Sassi, A. K. Ott, D. D. Fazio, D. Yoon, M. Amado, A. C. Ferrari, J. Linder, and J. W. A. Robinson, *p*-wave triggered superconductivity in single-layer graphene on an electron-doped oxide superconductor, Nat. Commun. **8**, 14024 (2017).

[44] G. C. Ménard, S. Guissart, C. Brun, M. Trif, F. Debontridder, R. T. Leriche, D. Demaille, D. Roditchev, P. Simon, and T. Cren, Two-dimensional topological superconductivity in Pb/Co/Si(111), Nat. Commun. **8**, 2040 (2017).

[45] M. Matsumoto and R. Heeb, Vortex charging effect in a chiral $p_x \pm ip_y$-wave superconductor, Phys. Rev. B **65**, 014504 (2001).

[46] The obtained phase diagrams (in scaled units) remain practically unchanged for a different choice of Fermi energy E_F and the coupling constant g, unless a particular choice leads to small values of $k_F \xi_0$—for which shape resonances of the order parameter are pronounced, the vortex states are strongly affected by those resonances [34], the vortex phase diagram becomes richer, and the delimiting lines in the phase diagram become less well defined.

[47] S.-I. Suzuki and Y. Asano, Spontaneous edge current in a small chiral superconductor with a rough surface, Phys. Rev. B **94**, 155302 (2016).

[48] A. Bouhon and M. Sigrist, Current inversion at the edges of a chiral *p*-wave superconductor, Phys. Rev. B **90**, 220511 (2014).

[49] V. V. Khotkevych, M. V. Milošević, and S. J. Bending, A scanning Hall probe microscope for high resolution magnetic imaging down to 300 mK, Rev. Sci. Instrum. **79**, 123708 (2008).

[50] P. J. Curran, S. J. Bending, W. M. Desoky, A. S. Gibbs, S. L. Lee, and A. P. Mackenzie, Search for spontaneous edge currents and vortex imaging in Sr_2RuO_4 mesostructures, Phys. Rev. B **89**, 144504 (2014).

[51] For a similar polarity-dependent effect on edge states due to the nearby (anti)parallel vortex, see Ref. [16].

[52] J. Garaud, J. Carlström, and E. Babaev, Topological Solitons in Three-Band Superconductors with Broken Time Reversal Symmetry, Phys. Rev. Lett. **107**, 197001 (2011).

[53] S. Gillis, J. Jäykkä, and M. V. Milošević, Vortex states in mesoscopic three-band superconductors, Phys. Rev. B **89**, 024512 (2014).

[54] A. Furusaki, M. Matsumoto, and M. Sigrist, Spontaneous Hall effect in a chiral *p*-wave superconductor, Phys. Rev. B **64**, 054514 (2001).

[55] J. B. Ketterson and S. N. Song, *Superconductivity* (Cambridge University, Cambridge, England, 1999).

[56] Y. Liu, Y. Zadorozhny, M. M. Rosario, B. Y. Rock, P. T. Carrigan, and H. Wang, Destruction of the global phase coherence in ultrathin, doubly connected superconducting cylinders, Science **294**, 2332 (2001).